

# Unraveling the optical contrast in $\text{Sb}_2\text{Te}$ and $\text{AgInSbTe}$ phase-change materials

Shehzad Ahmed<sup>1, 2</sup>, Xudong Wang<sup>1, 2\*</sup>, Yuxing Zhou<sup>1, 2</sup>, Liang Sun<sup>3</sup>, Riccardo Mazzarello<sup>4, 5\*</sup>, Wei Zhang<sup>1, 2\*</sup>

<sup>1</sup>State Key Laboratory for Mechanical Behavior of Materials, Center for Advancing Materials Performance from the Nanoscale, Xi'an Jiaotong University, Xi'an 710049, China

<sup>2</sup>Materials Studio for Neuro-Inspired Computing, Center for Alloy Innovation and Design (CAID), Xi'an Jiaotong University, Xi'an 710049, China

<sup>3</sup>Key Laboratory of Materials Processing Engineering, College of Materials Science and Engineering, Xi'an Shiyou University, Xi'an 710065, China

<sup>4</sup>Department of Physics, Sapienza University of Rome, 00185 Rome, Italy

<sup>5</sup>Institute for Theoretical Solid-State Physics, JARA-FIT and JARA-HPC, RWTH Aachen University, 52056 Aachen, Germany..

\*Emails: [xudong.wang@stu.xjtu.edu.cn](mailto:xudong.wang@stu.xjtu.edu.cn), [riccardo.mazzarello@uniroma1.it](mailto:riccardo.mazzarello@uniroma1.it), [wzhang0@mail.xjtu.edu.cn](mailto:wzhang0@mail.xjtu.edu.cn)

## Abstract

Chalcogenide phase-change materials (PCMs) show a significant contrast in optical reflectivity and electrical resistivity upon crystallization from the amorphous phase and are leading candidates for non-volatile photonic and electronic applications. In addition to the flagship  $\text{Ge}_2\text{Sb}_2\text{Te}_5$  phase-change alloy, doped  $\text{Sb}_2\text{Te}$  alloys, in particular  $\text{AgInSbTe}$  used in rewritable optical discs, have been widely investigated for decades, and nevertheless the theoretical insights on the optical properties of this important family of PCMs are scarce. Here, we carry out thorough ab initio simulations to gain an atomistic understanding of the optical properties of  $\text{Sb}_2\text{Te}$  and  $\text{AgInSbTe}$ . We show that the large optical contrast between the amorphous and crystalline phase stems from the change in bond type in the parent compound  $\text{Sb}_2\text{Te}$ . Ag and In impurities serve mostly the purpose of stabilization of the amorphous phase, and have marginal impact on the large variation in the dielectric function upon the phase transitions.

## I. Introduction

Phase-change materials (PCMs) undergo fast and reversible transitions between crystalline and amorphous states exhibiting electrical and optical contrast, enabling a number of important applications.[1-8] The first commercial products of PCMs were rewritable optical media (CD, DVD and Blu-ray Disc), which exploited the reflectivity contrast and employed laser pulses to switch the material.[9-11] More recently, the large resistance difference between the amorphous and crystalline phases is being exploited in electronic devices such as the 3D Xpoint non-volatile memories,[12-16] where electrical pulses are used to induce the structural transitions. Such devices offer an attractive combination of properties including excellent scalability, stability, high speed, and non-volatility.[17-23] PCMs are also promising for applications in neuro-inspired computing devices, aiming to eliminate the von Neumann bottleneck of traditional computing.[24-32] Very recently, with the booming development of optoelectronics and photonics, the optical properties of PCMs have gained again strong interests. In addition to photonic non-volatile memories[33-38] and neuro-inspired computing,[39-42] various emerging techniques based on PCMs have been proposed and demonstrated, such as non-volatile optoelectronic displays, reconfigurable optical metamaterials, mid-infrared absorbers, thermal emitters and others.[43-51]

Important families of PCMs are type I—the pseudo-binary Ge-Sb-Te alloys  $\text{GeTe}_{(1-x)}(\text{Sb}_2\text{Te}_3)_x$ , and type II—the doped  $\text{Sb}_x\text{Te}$  ( $x \geq 2$ ) binary compounds, such as Ag, In-doped  $\text{Sb}_2\text{Te}$ . Optical contrast in  $\text{Ge}_2\text{Sb}_2\text{Te}_5$  (GST) has been revealed to stem from a change in bonding mechanism.[52-57] The amorphous phase shows covalent bonding, whereas the crystalline, rocksalt-like structure displays metavalent bonding—MVB (previously known as resonant bonding), which is characterized by considerable electron delocalization.[58-63] In the metavalently bonded rocksalt phase, the  $p$  orbitals on neighboring atoms are aligned, which leads to the large matrix elements of the optical transitions and, thus, a large optical absorption. On the contrary, the disordering and the misalignment of the  $p$  orbitals in the amorphous state decreases the optical matrix elements and the absorption, resulting in the optical contrast. Although the family of doped  $\text{Sb}_x\text{Te}$  alloys has also been widely investigated for decades,[64-72] computational studies of the optical properties of  $\text{Sb}_2\text{Te}$  and  $\text{AgInSbTe}$  are scarce. Here we perform ab initio simulations based on density functional theory (DFT) to determine the dielectric function of crystalline and amorphous  $\text{Sb}_2\text{Te}$  and  $\text{AgInSbTe}$  and elucidate their optical contrast. Similarly to  $\text{GeSbTe}$  compounds, we find that the contrast can be ascribed to subtle changes in bonding.

## II. Methods

We carried out DFT-based ab initio molecular dynamics (AIMD) simulations using the second-generation Car-Parrinello molecular dynamics scheme[73] implemented in the CP2K package.[74] We employed the Perdew-Burke-Ernzerhof (PBE) functional[75] and the Goedecker pseudopotential.[76] The time step was set to 2 fs. The VASP package was also used to perform geometry relaxation and to compute the dielectric function. We employed the projector augmented wave (PAW) method[77] in combination with both PBE and hybrid Heyd-Scuseria-Ernzerhof (HSE06) functionals. [78] An energy cut off of 550 eV for plane waves was used to achieve the desired accuracy. The structural relaxation was carried out with the conjugate gradient (CG) method. A grid of  $15 \times 15 \times 3$  k-points was used for c- $\text{Sb}_2\text{Te}$  (whose primitive cell contains 9 atoms), whereas the  $\Gamma$  point approximation was used for the 216 atoms supercells of amorphous  $\text{Sb}_2\text{Te}$ , and crystalline and

amorphous  $\text{Ag}_8\text{In}_6\text{Sb}_{144}\text{Te}_{58}$ . The frequency-dependent dielectric matrix was calculated within the independent-particle approximation, without considering the local field effects and many body effects. This approximation was proven to be adequate to quantify the optical contrast between crystalline and amorphous GST.[55, 79] The dielectric function  $\epsilon(\omega)$  was determined in the energy interval of 0 to 7 eV. The imaginary part of  $\epsilon(\omega)$ , termed as  $\epsilon_2(\omega)$ , is given by

$$\epsilon_2(\omega) = \frac{4\pi^2 e^2}{\Omega} \lim_{q \rightarrow 0} \frac{1}{q^2} \times \sum_{c,v,\mathbf{k}} 2w_k \delta(E_c - E_v - \omega) |\langle c | \mathbf{e} \cdot \mathbf{q} | v \rangle|^2, \quad (1)$$

where  $\langle c | \mathbf{e} \cdot \mathbf{q} | v \rangle$  represents the joint optical transition from the states of the valence band ( $v$ ) to the states of the conduction band ( $c$ ),  $\mathbf{e}$  is the direction of polarization of the photon, and  $\mathbf{q}$  is the electron momentum operator.[80] The integration over the  $\mathbf{k}$ 's is a sum over special  $k$ -points with corresponding weighting factors  $w_k$ . In Formula (1), the matrix elements of the optical transitions are weighted by the Joint Density of States (JDOS) defined as:[81]

$$J(\omega) = 2 \sum_{v,c,\mathbf{k}} w_k \delta(E_c - E_v - \omega), \quad (2)$$

where  $E_v$  and  $E_c$  indicate the energies of the states in the valence and conduction bands, respectively.

### III. RESULTS AND DISCUSSIONS

Crystalline (c-)  $\text{Sb}_2\text{Te}_3$  forms a rhombohedral structure (space group  $\bar{P}3m1$ ) with alternate stacking of one  $\text{Sb}_2\text{Te}_3$  quintuple-layer (QL) and two Sb bi-layers (BLs),[82, 83] as shown in Figure 1a. The DFT-optimized lattice parameters obtained by using the PBE functional are  $a = 4.36 \text{ \AA}$  and  $c = 17.77 \text{ \AA}$ . In the c- $\text{Sb}_2\text{Te}_3$ , both Sb and Te atoms form octahedral bonding patterns. All the atoms display deviations from the perfect octahedral sites due to the pronounced Peierls distortion, yielding long-short Sb-Sb and Sb-Te bonding pairs. The Sb-Sb bond distance between the two Sb BLs is  $3.43 \text{ \AA}$ , while the Sb-Te bond distance between the Sb BL and  $\text{Sb}_2\text{Te}_3$  QL is  $3.53 \text{ \AA}$ . The latter is smaller than the Te-Te bond distance between two QLs in rhombohedral  $\text{Sb}_2\text{Te}_3$ ,  $3.74 \text{ \AA}$ . [84] The structural gaps between QLs in rhombohedral  $\text{Sb}_2\text{Te}_3$  are regarded as pseudo-van der Waals (vdW) gaps due to the presence of weak covalent interactions.[85] In rhombohedral  $\text{Sb}_2\text{Te}_3$ , the smaller bond distance between the Sb BLs and  $\text{Sb}_2\text{Te}_3$  QL indicates stronger covalent interaction.

We carried out AIMD simulations to generate amorphous (a-)  $\text{Sb}_2\text{Te}_3$  models following the standard melt-quench protocol.[86] 144 Sb atoms and 72 Te atoms were placed in a cubic box, and were heated up to 3000 K to remove all possible crystalline order. The disordered model was then quenched down to and equilibrated at 1000 K over 30 ps, and was then quenched down to 300 K in 50 ps. After 30 ps equilibration at 300 K, the amorphous model was further quenched down to 0 K for electronic structure analyses and optical property calculations. The theoretical value of the supercell parameter is  $\sim 19.77 \text{ \AA}$ , corresponding to a density of  $5.74 \text{ g/cm}^3$ . A snapshot of amorphous  $\text{Sb}_2\text{Te}_3$  is shown in Figure 1b.

The crystalline and amorphous structures shown in Figure 1a-b were then used for the calculation of the electronic density of states (DOS). Besides the PBE functional, the hybrid HSE06 scheme was also employed to compute this quantity, since the latter typically gives more accurate band gap size. As

shown in Figure 1c, a narrow band gap is present for both the crystalline and amorphous  $\text{Sb}_2\text{Te}$ . The gap size of c- $\text{Sb}_2\text{Te}$  (0.19 eV, HSE06) is smaller than that of a- $\text{Sb}_2\text{Te}$  (0.58 eV, HSE06).

Figure 2a shows the imaginary part of the dielectric functions  $\epsilon_2$  (i.e. the optical absorption) of crystalline and amorphous  $\text{Sb}_2\text{Te}$ . Significant differences are found between the two phases using either the PBE or the HSE06 functional. The  $\epsilon_2$  of the crystalline phase is much higher than that of the amorphous phase in the photon energy range from 0 eV to 3 eV, covering nearly the whole visible light spectrum (1.64-3.19 eV). The peak value of the amorphous  $\epsilon_2$  curve is reduced by nearly three times and the peak position is shifted towards higher energies by  $\sim 0.5$  eV with respect to those of the crystalline  $\epsilon_2$  curve. To explain this large contrast in  $\epsilon_2$ , we compared the JDOS of the two phases in Figure 2b. The JDOS of c- $\text{Sb}_2\text{Te}$  is larger than that of a- $\text{Sb}_2\text{Te}$  in the energy range from 0 eV to 1 eV due to its smaller band gap, while the two curves approach each other at higher photon energies. Therefore, the JDOS alone cannot explain the large differences in  $\epsilon_2$  in the energy range from 1 eV to 3 eV.

The observed optical contrast in  $\text{Sb}_2\text{Te}$  is qualitatively similar to that found in GST. The latter was explained by the transition from MVB to covalent bonding upon amorphization of GST. In rocksalt GST, there are on average 3  $p$  electrons per lattice site (including 10% vacant sites), and the  $p$  orbital alignment promotes electron delocalization, thus the large dielectric constant.[52] In contrast, amorphous GST is characterized by strong angular disorder between pairs of bonds,[55] which leads to  $p$  orbital misalignment and covalent bonding, largely reducing the dielectric constant.[87] In fact, simulations showed that pronounced optical contrast is also obtained between two different crystalline structures of the parent PCM GeTe—the stable rhombohedral phase versus a hypothetical orthorhombic phase where strong  $p$  orbital misalignment occurs.[54]

The angular distribution function (ADF) of a- $\text{Sb}_2\text{Te}$  is shown in Figure 3a. Octahedral bonds are typically found for both Sb and Te atoms with nearly  $90^\circ$  bond angles. On average Sb atoms have more neighbors ( $\sim 4$ ) than Te atoms ( $\sim 3$ ). The nearly aligned bond pairs result in an additional peak in ADF near  $180^\circ$ . Thorough structural analyses of a- $\text{Sb}_2\text{Te}$ , including radial distribution function, coordination number, primitive rings statistics as well as cavity distribution, can be found in our earlier work.[88] Here, we focus on the bond alignment analysis. We first calculate the angular-limited three-body correlation (ALTBC)[89] to gain an overview about the bond correlation in a- $\text{Sb}_2\text{Te}$ . We regard a pair of bonds with bond angle larger than  $160^\circ$  as a nearly aligned bond pair. The long/short bond pattern around all Sb atoms in a- $\text{Sb}_2\text{Te}$  is mapped out in Figure 3b, showing a peak center around 2.9/3.5 Å. In c- $\text{Sb}_2\text{Te}$ , three long/short bond correlations are present, namely, 3.04/3.20 Å for the Te-Sb-Te bond pair in the  $\text{Sb}_2\text{Te}_3$  QL, 2.96/3.43 Å for the Sb-Sb-Sb bond pair in the Sb BLs, and 2.96/3.53 Å for the Te-Sb-Sb bond pair between the QL and BL.

Next, we quantify the degree of angular disorder by analyzing the length of chains of aligned bond pairs. We use a large distance cutoff 3.6 Å for such analysis, covering the majority of long bonds (Figure 3b). Typical aligned bond chains are highlighted in Figure 3c. The detailed counting in Figure 3d shows that only  $\sim 18\%$  of such chains can contain more than 3 atoms. The longest chain is identified to have 6 atoms. The angular distortion of these chains shows a broad distribution between  $160^\circ$  and  $180^\circ$  (Figure 3d inset). However, in c- $\text{Sb}_2\text{Te}$ , despite slight angular distortions about  $15^\circ$  (as marked

by blue dashed lines in Figure 3d inset), all the aligned bond chains are highly extended. Only lattice defects or grain boundaries can break these highly aligned bond chains. c-Sb<sub>2</sub>Te with both Sb BLs and Sb<sub>2</sub>Te<sub>3</sub> QL shows on average 3 *p* electrons per lattice site locally, promoting electron delocalization and MVB. While in a-Sb<sub>2</sub>Te, despite all atoms are octahedrally bonded, the strong angular disorder between these local motifs breaks the aligned bond chains, displaying conventional covalent bonding with poor electron delocalization.

Then we investigate the effects of Ag and In impurities on the optical properties. We chose a Ag<sub>8</sub>In<sub>6</sub>Sb<sub>144</sub>Te<sub>58</sub> model (abbreviated as AIST in the following), which has a composition very close to the previous experimental and AIMD work presented in Refs. [69, 70] Since, for such composition, the ratio between Sb and Te atoms is about 2.48, Ag and In impurities are likely to occupy the positions of Te atoms in c-Sb<sub>2</sub>Te. Figure 4a shows one possible c-AIST structure. The supercell was fully relaxed with the PBE functional. A cubic supercell with 216 atoms and the exact chemical composition was used to simulate the amorphous phase. Following the same melt-quench protocol, a-AIST was obtained, as shown in Figure 4b. These two atomic structures were then used for electronic structure calculations. The corresponding DOS plots are shown in Figure 4c. The presence of Ag and In impurities tends to reduce the size of band gap in both c-AIST (0.15 eV, HSE06) and a-AIST (0.43 eV, HSE06). The calculated band gap values of both phases are in good agreement with experimental values.[90, 91]

Figure 5a shows the dielectric function  $\epsilon_2$  of crystalline and amorphous AIST. The peak height is reduced by ~24% (HSE06 data) for c-AIST with respect to c-Sb<sub>2</sub>Te (the trend is the same for PBE data). This is due to the fact that the presence of Ag and In impurities breaks the alignment of *p* orbitals in the crystalline phase, as Ag and In have, respectively, zero and one *p* electron in their valence shell. These impurities result in a weakening of MVB, and thereby a reduction of the dielectric function. Upon alloying the amorphous phase, the peak height of  $\epsilon_2$  is reduced by ~9% (HSE06 data) and the peak position is also shifted towards higher energies by 0.25 eV (HSE06 data). The change in  $\epsilon_2$  brought about by the impurities is smaller in the amorphous phase: this can be attributed to the fact that the aligned bond chains are anyway short in the amorphous phase. As regards the JDOS (Figure 5b), the difference between the crystalline and amorphous phase below 2 eV is more pronounced in AIST than in Sb<sub>2</sub>Te, primarily because a very small band gap is found in c-AIST.

At last, we note that the c-AIST structure considered here was chosen to resemble the ordered c-Sb<sub>2</sub>Te as much as possible to assess the impurity effects. In fact, simulations showed that, at elevated temperatures, AIST crystallizes on a nanosecond time scale in a A7 structure with random occupation of all four elements.[68, 70] It is expected that even Sb<sub>2</sub>Te crystallizes into a phase with strong substitutional Sb/Te disorder at high temperature. Upon long-term thermal annealing over hours, the Sb and Te atoms (and, possibly, the impurity atoms as well) can further rearrange to form a more stable structure with higher chemical order.[92] Nevertheless, the effects of Ag and In impurities should qualitatively be the same in the disordered crystalline phases, namely, breaking the aligned bond chains due to the shortage of *p* electrons.

## VI. CONCLUSION

In summary, we performed thorough DFT and AIMD simulations to investigate the optical contrast between amorphous and crystalline Sb<sub>2</sub>Te and AIST. We showed that the large imaginary part of the dielectric function in c-Sb<sub>2</sub>Te stems from highly extended bond chains of aligned *p* orbitals with 3 *p* electrons per lattice site on average, promoting electron delocalization and the formation of metavalent bonding. In contrast, despite strong angular disorder is present in a-Sb<sub>2</sub>Te, breaking the aligned bond chains into small pieces and turning the bonding pattern into conventional covalent bonding. In addition, we assessed the impurity effects of common alloy elements, namely, Ag and In, which result in a moderate weakening of absorption due to the breaking of the alignment of *p* orbitals in the crystalline phase. In spite of this, a significant optical contrast is also observed between crystalline and amorphous AIST. We conclude that the optical contrast in type II PCM originates mostly from its parent phase but not from the impurity atoms. Too large Ag and In doping could even be detrimental because of their stronger impact on the dielectric function of the crystalline state. Thus, the impurities serve only the purpose of enhancing the amorphous stability for practical applications.

## References

- [1] Wuttig M and Yamada N 2007 *Nat. Mater.* **6** 824-832.
- [2] Zhang W, Mazzarello R, Wuttig M and Ma E 2019 *Nat. Rev. Mater.* **4** 150-168.
- [3] Zhang W, Mazzarello R and Ma E 2019 *MRS Bulletin* **44** 686-690.
- [4] Wright D, Bhaskaran H and Pernice W 2019 *MRS Bulletin* **44** 721-725.
- [5] Wuttig M, Bhaskaran H and Taubner T 2017 *Nat. Photon.* **11** 465-476.
- [6] Gholipour B 2019 *Science* **366** 186-187.
- [7] Zhang Z, Wang Z, Shi T, Bi C, Rao F, Cai Y, Liu Q, Wu H and Zhou P 2020 *InfoMat.* **2** 261-290.
- [8] Zhang W and Ma E 2020 *Mater. Today* **41** 156-176.
- [9] Yamada N, Ohno E, Akahira N, Nishiuchi K, Nagata K and Takao M 1987 *Jpn. J. Appl. Phys. Part 1* **26** 61- 66.
- [10] Yamada N, Ohno E, Nishiuchi K, Akahira N and Takao M 1991 *J. Appl. Phys.* **69** 2849-2856.
- [11] Yamada N and Matsunaga T 2000 *J. Appl. Phys.* **88** 7020-7028.
- [12] Choe J, Intel 3D XPoint Memory Die Removed from Intel Optane™ PCM (Phase Change Memory). <http://www.techinsights.com/about-techinsights/overview/blog/intel-3d-xpoint-memory-die-removed-from-intel-optane-pcm/>
- [13] Fong S W, Neumann C M and Wong H-S P 2017 *IEEE Trans. Electron. Dev.* **64** 4374-4385.
- [14] Yeh C W, et al. 2018 *VLSI Tech. Dig.* pp.205-206.
- [15] Chien W C, et al. 2019 *VLSI Tech. Dig.* pp.T60-T61.
- [16] Li X-B, Chen N-K, Wang X-P and Sun H-B 2018 *Adv. Funct. Mater.* **28** 1803380.
- [17] Wong H-S P, Raoux S, Kim S B, Liang J, Reifenberg J P, Rajendran B, Asheghi M and Goodson K E 2010 *Proc. IEEE* **98** 2201.
- [18] Raoux S, Welnic W and Ielmini D 2010 *Chem. Rev.* **110** 240-267.
- [19] Zhang W and Wuttig M 2019 *Phys. Status Solidi RRL* **13** 1900130.
- [20] Rao F, et al. 2017 *Science* **358** 1423-1427.
- [21] Ding K, et al. 2019 *Science* **366** 210-215.
- [22] Sun Z, Zhou J and Ahuja R 2006 *Phys. Rev. Lett.* **96** 055507.
- [23] Fantini P 2020 *J. Phys. D: Appl. Phys.* **53** 283002.
- [24] Kuzum D, Jeyasingh R G, Lee B and Wong H S P 2012 *Nano Lett.* **12** 2179-2186.

- [25] Wright C D, Liu Y, Kohary K I, Aziz M M and Hicken R J 2011 *Adv. Mater.* **23** 3408-3413.
- [26] Wright C D, Wang L, Aziz M M, Diosdado J A V and Ashwin P 2012 *Phys. Status Solidi B* **249** 1978-1984.
- [27] Cassinerio M, Ciocchini N and Ielmini D 2013 *Adv. Mater.* **25** 5975-5980.
- [28] Sebastian A, Le Gallo M, Burr G W, Kim S, BrightSky M and Eleftheriou E 2018 *J. Appl. Phys.* **124** 111101.
- [29] Sebastian A, Le Gallo M, Khaddam-Aljameh R and Eleftheriou E 2020 *Nat. Nanotechnol.* **15** 529-544.
- [30] Ielmini D and Wong H-S P 2018 *Nat. Electron.* **1** 333-343.
- [31] Xu M, et al. 2020 *Adv. Funct. Mater.* **30** 2003419.
- [32] Lee T H, Loke D, Huang K J, Wang W J and Elliott S R 2014 *Adv. Mater.* **26** 7493-7498.
- [33] Ríos C, Hosseini P, Wright C D, Bhaskaran H and Pernice W H 2014 *Adv. Mater.* **26** 1372-1377.
- [34] Ríos C, Stegmaier M, Hosseini P, Wang D, Scherer T, Wright C D, Bhaskaran H and Pernice W H P 2015 *Nat. Photon.* **9** 725-732.
- [35] Cheng Z, Rios C, Youngblood N, Wright C D, Pernice W H P and Bhaskaran H 2018 *Adv. Mater.* **30** 1802435.
- [36] Zhang Q, Zhang Y, Li J, Soref R, Gu T and Hu J 2018 *Opt. Lett.* **43** 94-97.
- [37] Zhang Y, et al. 2019 *Nat. Commun.* **10** 4279.
- [38] Zhang H, Zhou L, Lu L, Xu J, Wang N, Hu H, Rahman B M A, Zhou Z and Chen J 2019 *ACS Photon.* **6** 2205-2212.
- [39] Cheng Z, Ríos C, Pernice W H P, Wright C D and Bhaskaran H 2017 *Sci. Adv.* **3** e1700160.
- [40] Feldmann J, Stegmaier M, Gruhler N, Rios C, Bhaskaran H, Wright C D and Pernice W H P 2017 *Nat. Commun.* **8** 1256.
- [41] Ríos C, Youngblood N, Cheng Z, Gallo M L, Pernice W H P, Wright C D, Sebastian A and Bhaskaran H 2019 *Sci. Adv.* **5** eaau5759.
- [42] Feldmann J, Youngblood N, Wright C D, Bhaskaran H and Pernice W H P 2019 *Nature* **569** 208-214.
- [43] Hosseini P, Wright C D and Bhaskaran H 2014 *Nature* **511** 206-211.
- [44] Carrillo S G C, Trimby L, Au Y Y, Nagareddy V K, Rodriguez-Hernandez G, Hosseini P, Ríos C, Bhaskaran H and Wright C D 2019 *Adv. Opt. Mater.* **7** 1801782.
- [45] Wang Q, Rogers E T F, Gholipour B, Wang C-M, Yuan G, Teng J and Zheludev N I 2015 *Nat. Photon.* **10** 60-65.
- [46] Hafermann M, Schöppe P, Rensberg J and Ronning C 2018 *ACS Photon.* **5** 5103-5109.
- [47] Tittl A, et al. 2015 *Adv. Mater.* **27** 4597-4603.
- [48] Cao T, et al. 2018 *Adv. Opt. Mater.* **6** 1800169.
- [49] Li P, Yang X, Mass T W, Hanss J, Lewin M, Michel A U, Wuttig M and Taubner T 2016 *Nat. Mater.* **15** 870-875.
- [50] Tian J, Luo H, Yang Y, Ding F, Qu Y, Zhao D, Qiu M and Bozhevolnyi S I 2019 *Nat. Commun.* **10** 396.
- [51] Zhang H, Zhou L, Xu J, Wang N, Hu H, Lu L, Rahman B M A and Chen J 2019 *Sci. Bull.* **64** 782-789.
- [52] Shportko K, Kremers S, Woda M, Lencer D, Robertson J and Wuttig M 2008 *Nat. Mater.* **7** 653-658.
- [53] Lencer D, Salinga M, Grabowski B, Hickel T, Neugebauer J and Wuttig M 2008 *Nat. Mater.* **7** 972-977.
- [54] Huang B and Robertson J 2010 *Phys. Rev. B* **81** 081204(R).
- [55] Caravati S, Bernasconi M and Parrinello M 2010 *J. Phys. Condens. Matter.* **22** 315801.
- [56] Wełnic W, Botti S, Reining L and Wuttig M 2007 *Phys. Rev. Lett.* **98** 236403.
- [57] Xu M, Cheng Y, Sheng H and Ma E 2009 *Phys. Rev. Lett.* **103** 195502.
- [58] Wuttig M, Deringer V L, Gonze X, Bichara C and Raty J Y 2018 *Adv. Mater.* **30** 1803777.
- [59] Zhu M, Cojocaru-Mirédin O, Mio A M, Keutgen J, Küpers M, Yu Y, Cho J-Y, Dronskowski R and Wuttig M 2018 *Adv. Mater.* **30** 1706735.
- [60] Raty J Y, Schumacher M, Golub P, Deringer V L, Gatti C and Wuttig M 2019 *Adv. Mater.* **31** 1806280.
- [61] Maier S, et al. 2020 *Adv. Mater.* **32** 2005533.
- [62] Kooi B J and Wuttig M 2020 *Adv. Mater.* **32** 1908302.
- [63] Cheng Y, et al. 2019 *Adv. Mater.* **31** 1904316.
- [64] Iwasaki H, Harigaya M, Nonoyama O, Kageyama Y, Takahashi M, Yamada K, Deguchi H and Ide Y 1993 *Jpn. J. Appl.*

*Phys. Part 1* **32** 5241-5247.

- [65] Matsunaga T, Umetani Y and Yamada N 2001 *Phys. Rev. B* **64** 184116.
- [66] van Pieterse L, Lankhorst M H R, van Schijndel M, Kuiper A E T and Roosen J H J 2005 *J. Appl. Phys.* **97** 083520.
- [67] Lankhorst M H R, Ketelaars B W and Wolters R A 2005 *Nat. Mater.* **4** 347-352.
- [68] Matsunaga T, et al. 2011 *Nat. Mater.* **10** 129-134.
- [69] Salinga M, Carria E, Kaldenbach A, Bornhofft M, Benke J, Mayer J and Wuttig M 2013 *Nat. Commun.* **4** 2371.
- [70] Zhang W, Ronneberger I, Zalden P, Xu M, Salinga M, Wuttig M and Mazzarello R 2014 *Sci. Rep.* **4** 6529.
- [71] Zalden P, et al. 2019 *Science* **364** 1062–1067.
- [72] Akola J and Jones R O 2009 *Appl. Phys. Lett.* **94** 251905.
- [73] Kühne T, Krack M, Mohamed F and Parrinello M 2007 *Phys. Rev. Lett.* **98** 066401.
- [74] Hutter J, Iannuzzi M, Schiffmann F and VandeVondele J 2014 *WIREs Comput. Mol. Sci.* **4** 15-25.
- [75] Perdew J P, Burke K and Ernzerhof M 1996 *Phys. Rev. Lett.* **77** 3865-3868.
- [76] Goedecker S, Teter M and Hutter J 1996 *Phys. Rev. B* **54** 1703.
- [77] Blöchl P E 1994 *Phys. Rev. B* **50** 17953-17979.
- [78] Heyd J, Scuseria G E and Ernzerhof M 2006 *J. Chem. Phys.* **124** 219906.
- [79] Wełnic W, Wuttig M, Botti S and Reining L 2009 *Comptes Rendus Physique* **10** 514-527.
- [80] Gajdoš M, Hummer K, Kresse G, Furthmüller J and Bechstedt F 2006 *Phys. Rev. B* **73** 045112
- [81] Wang V, Xu N, Liu J C, Tang G and Geng W-T 2019 *arXiv:1908.08269*.
- [82] Agafonov V and Rodier N 1991 *Acta Cryst.* **C47** 1141-1143.
- [83] Kifune K, Kubota Y, Matsunaga T and Yamada N 2005 *Acta Cryst.* **B61** 492-497.
- [84] Anderson T L and Krause H B 1974 *Acta Crystallogr. B* **30** 1307-1310.
- [85] Wang R, Lange F R L, Cecchi S, Hanke M, Wuttig M and Calarco R 2018 *Adv. Funct. Mater.* **28** 1705901.
- [86] Zhang W, Deringer V L, Dronskowski R, Mazzarello R, Ma E and Wuttig M 2015 *MRS Bulletin* **40** 856-865.
- [87] Chen C, et al. 2017 *Phys. Rev. B* **95** 094111.
- [88] Zhang W, Ronneberger I, Li Y and Mazzarello R 2014 *Chem. Month.* **145** 97-101.
- [89] Raty J-Y, Zhang W, Luckas J, Chen C, Bichara C, Mazzarello R and Wuttig M 2015 *Nat. Commun.* **6** 7467.
- [90] Shukla K D, Sahu S, Manivannan A and Deshpande U P 2017 *Phys. Status Solidi RRL* **11** 1700273.
- [91] Rutten M, Kaes M, Albert A, Wuttig M and Salinga M 2015 *Sci. Rep.* **5** 17362.
- [92] Zhu M, et al. 2019 *Nat. Commun.* **10** 3525.

## Acknowledgments

W.Z. thanks the support of National Natural Science Foundation of China (61774123) and 111 Project 2.0 (BP2018008). S.A. acknowledges scholarship support from Chinese Scholarship Council. R.M. acknowledges funding from Deutsche Forschungsgemeinschaft (DFG) within SFB 917 ("Nanoswitches"). W.Z. acknowledges the support by the HPC platform of Xi'an Jiaotong University, and the International Joint Laboratory for Micro/Nano Manufacturing and Measurement Technologies of Xi'an Jiaotong University.



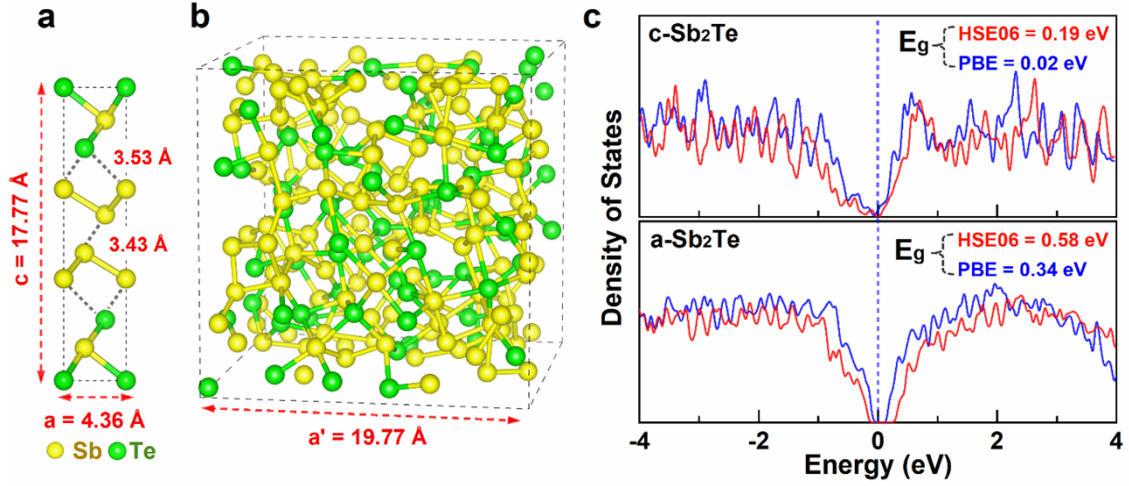


**Figure 1:** (a) The crystalline structure of rhombohedral  $\text{Sb}_2\text{Te}$  upon DFT-PBE relaxation. (b) The amorphous structure of  $\text{Sb}_2\text{Te}$  by melt-quenched AIMD simulation. Sb and Te atoms are rendered with yellow and green spheres. (c) Density of states (DOS) of crystalline and amorphous  $\text{Sb}_2\text{Te}$  calculated with both PBE and HSE06 functionals.

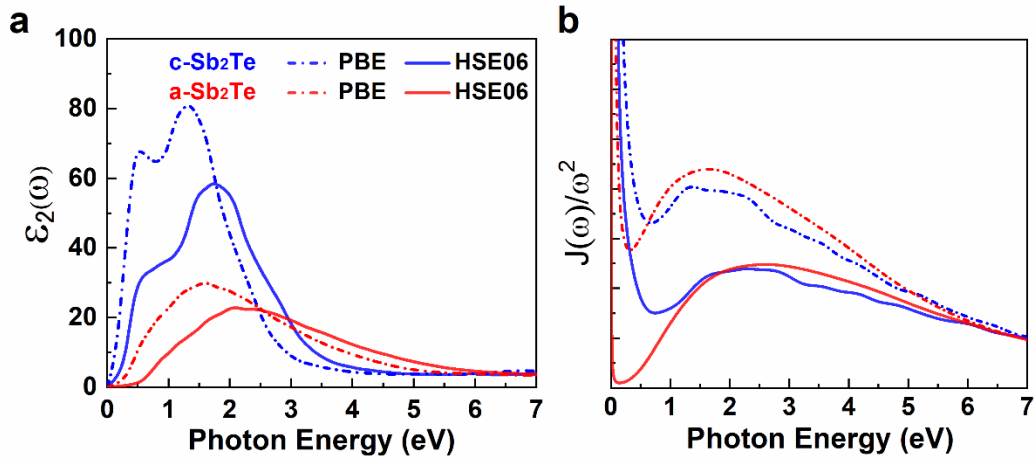


**Figure 2:** (a) Imaginary part of the dielectric function  $\epsilon_2$  and (b)  $J(\omega)/\omega^2$  of the amorphous (red lines) and crystalline (blue lines) phases of  $\text{Sb}_2\text{Te}$ . Dashed and solid lines represent results calculated with PBE and HSE06 functionals, respectively.

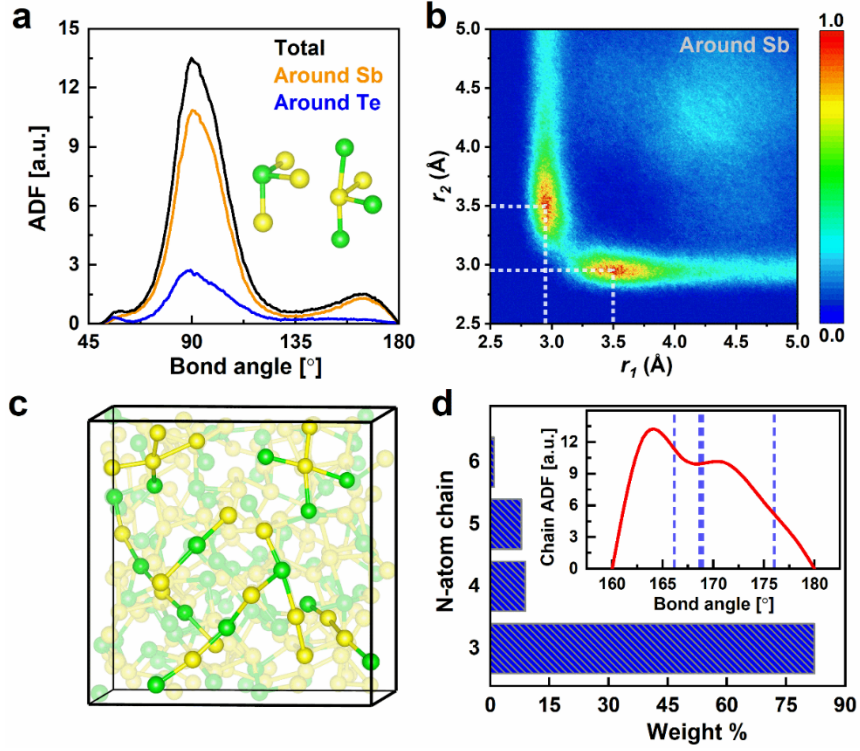


**Figure 3:** (a) The angle distribution function (ADF) and (b) the angular-limited three-body correlation (ALTBC) of a-Sb<sub>2</sub>Te with bond angle larger than 160°. Data were collected at 300 K over 15 ps. (c) A snapshot of a-Sb<sub>2</sub>Te at 0 K highlights the long/short bond chains. (d) The corresponding analysis on chain length of nearly aligned bond pairs. The inset shows the ADF of the aligned bond chains. The dashed lines mark the ADF of the aligned bond chains in c-Sb<sub>2</sub>Te.

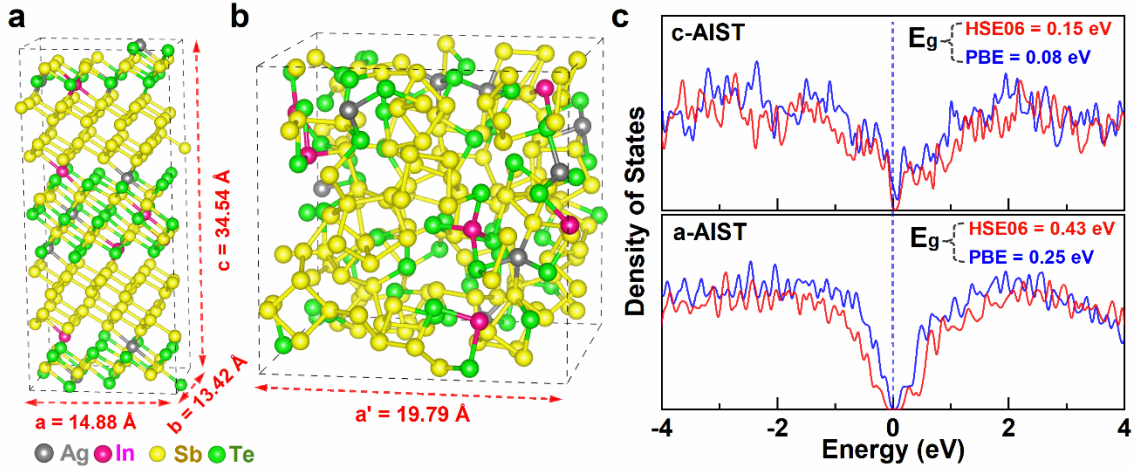


**Figure 4:** Atomic structures of (a) crystalline and (b) amorphous AIST. Ag, In, Sb and Te atoms are rendered with silver, pink, yellow and green spheres. (c) Electronic DOS of crystalline and amorphous AIST calculated with both PBE and HSE06 functionals.

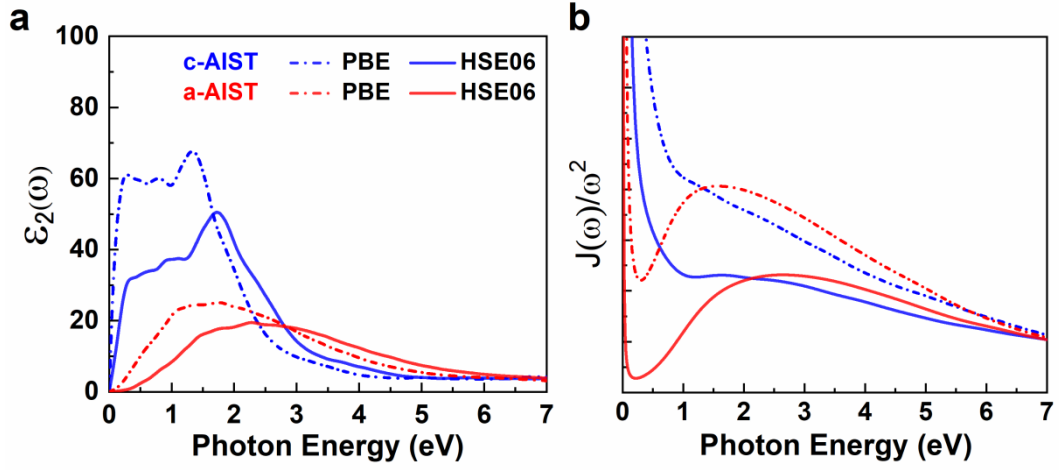


**Figure 5:** (a) Imaginary part of the dielectric function  $\epsilon_2$  and (b)  $J(\omega)/\omega^2$  of the amorphous (red lines) and crystalline (blue lines) phases of AIST. Dashed and solid lines represent results calculated with both PBE and HSE06 functionals, respectively.